XVI International Conference on Durability of Building Materials and Components
DBMC 2023, China
K.F. Li and D.P. Fang (Eds)

Rebar-matrix Interface in Extrusion Molded Cementitious Filaments

Rijiao Yang [1, 2], Qiang Zeng [1]*, Zhendi Wang [2]

[1]College of Civil Engineering and Architecture, Zhejiang University, Hangzhou, 310058, China, 12212088@zju.edu.cn (Rijiao Yang), cengq14@zju.edu.cn(Qiang Zeng)

[2] State Key Laboratory of Green Building Materials, China Building Materials Academy, Beijing 100024, P.R. China,wzhendi@163.com(Zhendi Wang)

Abstract.*Extrusion molding enables automatic construction through the pattern of material addition. The unique molding would result in several features that are different from those in conventional framework molding, such as weak interlayer bonding and a laminar structure with high anisotropy. To strengthen the interlayer bonding, reinforcement is often implanted to penetrate through the extrusion molded filaments (EMF). However, different from the pre-implantation of reinforcement before concrete casting, the post-implantation of reinforcement in EMF may trigger the problems concerning the interface bonding between reinforcement and material matrix. In this work, saddle stitches, a type of U-shape rebar or fiber, are taken as an example to demonstrate the effect of the post-implantation of reinforcement on the interfacial structure between the rebar and EMF matrix. X-ray computed tomography (XCT) is employed to non-destructively probe the post-implanted saddle stitches as well as the surrounded EMF materials. Regions of interest (ROI) are set on the rebar-matrix interfaces to elaborately analyze the material or defect distributions around the saddle stitches. Results demonstrate that insufficient material filling is observed at the outboard of the U-shape rebar, while material pressing is shown at the inboard. Large defects unevenly form in the rebar-matrix interface. Mechanisms of the observations may be ascribed to the low flowability of EMF materials that can hardly migrate to the rebar-matrix interfacial gaps spontaneously. The findings would deepen the understandings in rebar-matrix interfacial structure of EMF with post-implantation of reinforcement.*

Keywords:*Extrusion;Saddle stitches;XCT; Bonding; Defects;*

1 Introduction

Concrete extrusion molding, one of the most used three-dimensional (3D) printing patterns, has brought great advances to automatic constructions [Arunothayan et al. 2021, Wang et al. 2020, Li et al. 2022]. However, the layer-by-layer addition of extrusion molding can result in anisotropic structure with weak interlayer bonding [Nerella et al. 2019, Ding et al. 2020]. To strengthen the interlayer bonding between the extrusion molded concrete filaments, many techniques have been proposed, such as adjusting printing parameters, changing mix proportions, spraying interface strengthening agency and implanting reinforcement [Lu et al. 2019, Cao et al. 2022]. The implantation of reinforcement through the extrusion molded filaments (EMFs) may be the most effective way for interface strength enhancement. In this work, we used a post-implantation method to reinforce EMFs, which is different from traditional concrete reinforcement, where the reinforcement is pre-implanted and the concrete is sufficiently vibrated after cast, so the concrete slurries fully fill the space around the reinforcement. On one hand, the reinforcement is usually implanted through several layers, which would disturb the originally printed structure [Wang et al. 2021]. On the other hand, the

EMF structure will not be vibrated to avoid the possible collapse of the 3D printed concrete [Sun et al. 2022]. In this case, concrete slurries will not flow to fill the space around the rebars. Therefore, the post-implantation of reinforcement in EMF may lead to the formation of defects between the rebars and material matrix.

This work mainly focuses on the interface structure between post-implanted rebars and cement matrix. Cementitious slurries with three viscosities were controlled to prepare the EMFs. Saddle stitches, a type of U-shape rebar, were taken as the reinforcement. X-ray computed tomography (XCT) was employed to non-destructively probe the post-implanted saddle stitches as well as the surrounded EMF materials. The defects around the saddle stitches were extracted and the mechanisms were discussed.

2 Sample and Method

Three mix proportions were designed to control the slurries' viscosity (**Table 1**). A Portland cement (Type PI 42.5) was used as the binder for EMFs fabrication. The mix proportions of EMFs were set as follows: water-to-cement (w/c) ratio of 0.3, sand-to-cement (s/c) ratio of 0.8, polycarboxylate superplasticizer (PCE-SP) of 0.3 wt%, and alkali accelerator of 1.2 wt%. To tune the EMF slurries' viscosity, hydroxypropyl methylcellulose (HPMC) of 0.2, 0.3 and 0.4 wt% (in reference to cement weight) were used.

Table 1 Mix proportions of the 3D-printed extrusion molded cementitious filaments (EMFs)

Sample ID	Cement /wt%	Water /wt%	Sand /wt%	Accelerator /wt%	HPMC /wt%	PCE-SP /wt%
EMF-02	100	30	80	1.2	0.2	0.3
EMF-03	100	30	80	1.2	0.3	0.3
EMF-04	100	30	80	1.2	0.4	0.3

EMFs were printed by a homemade 3D printing machine with the parameters shown as follows, printing speed of 30 mm/s, filament height of 20 mm, length of 200 mm. Saddle stitches with 40 mm in length, 20 mm in width and 3.0 mm in diameter were implanted into the EMFs to enhance interlayer bonding (**Figure 1a**). After two layers of EMFs were finished, the saddle stitches were manually placed in the filaments every 30 mm, and the last layer of filament was extruded to cover the saddle stitches (**Figure 1b**). After primary hardening for 24 h, the EMFs were cured for 28 d in a standard curing condition. Later, the specimens were cut into small segments containing two saddle stitches for XCT scan test.

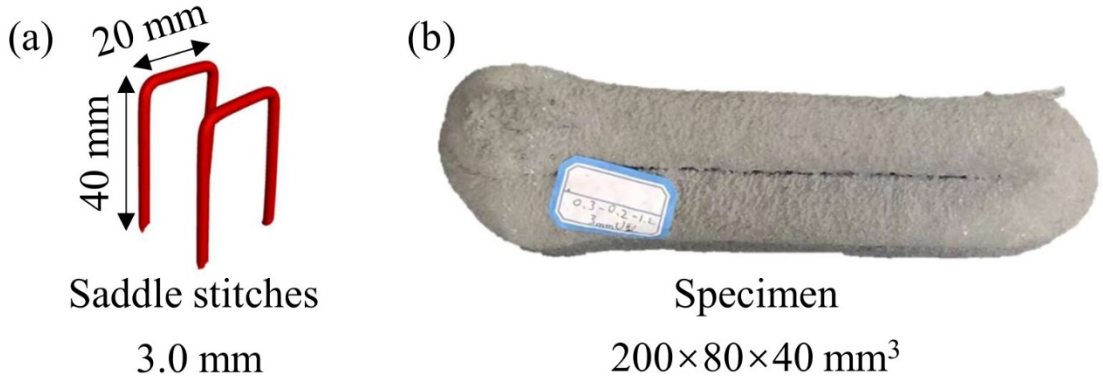

Figure 1 (a) Illustration of two saddle stitches, (b) image of an EMF specimen

The prepared EFM segments were put into a XTH255/320 LC (Nikon, Japan) device for non-destructive XCT scans (**Figure 2a**). Each segment was fixed on the sample frame between the X-ray emitter and the detector with the pixels of 2000×2000. The parameters of XCT test were set as 140 kV and 160 μA. A thin Cu film of 0.25 mm was attached on the tube to filter the noises of X-ray beams. The exposure time was set as 708 ms, and 2000 X-ray projections with the resolution of 36.5 μm/pixel were obtained in 23.6 min. All projections were qualified and reconstructed by "CT 3D Pro" software (**Figure 2b**). After reconstruction, the digital data was imported into "VG Studio" for further analysis (**Figure 2c**) [Yang et al. 2022].

A region of interest (ROI) of 8.5mm in diameter was extracted to contain the saddle stitches and the surrounding phases. A gray value threshold was applied to reconstruct the saddle stitches (**Figure 2d**). However, due to the artifacts [Aleksejev et al. 2022], the direct gray value thresholding method can not allow us to acquire the phases of low density around the saddle stiches of high density. Therefore, a specifically designed method was applied. First, the saddle stitches were first removed or set as pores, and expanded to include the region in 2 mm. Analysis based on gray value threshold was performed again to reconstruct the phases around the saddle stitches. The "pore analysis module" was used to measure the volume, and fraction of the phase identified (**Figure 2e**).

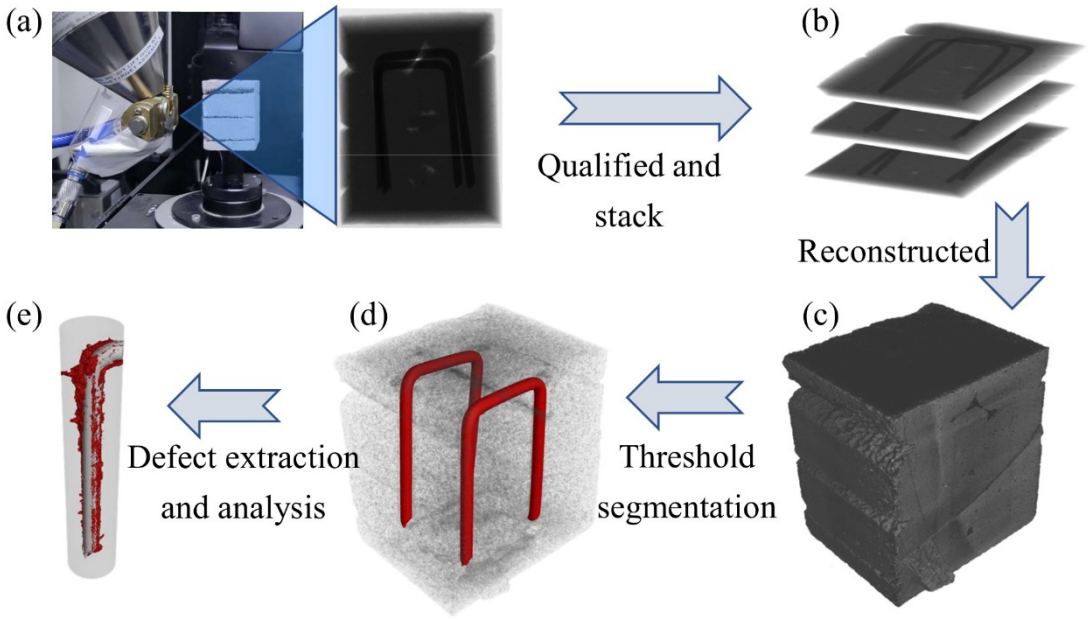

Figure 2 Test and data processing by micro-XCT: (a) XCT scans of an EMF segment with two saddle stitches; (b) image stacked in "CT3DPro" software; (c) 3D image of the sample in "VG Studio" software; (d) 3D image of the saddle stitches in the sample; (e) identification of the phase around saddle stitches.

3 Results and discussion

Figure 3a representatively shows the 3D structure of a selected ROI with three different phases in EMF-02, EMF-03 and EMF-04: rebar (gray), cement matrix (transparent), and pores (red). Those pores are large and connected, which may be diagnosed as defects. More connected defects are observed at the outboard of the U-shape rebar, while material pressing is shown at the inboard. **Figure 3b** shows the volume fraction of those defects at different positions. The volume fraction of the defects was about 10% at the bottom of the saddle stitches, and progressively increased to about 50% at the top. It can be found in **Figure 3b** that with increasing the cement slurries' viscosity, the volume fraction of defects rose, because the increased cohesive forces between cement particles enhanced the resistance against material flow.

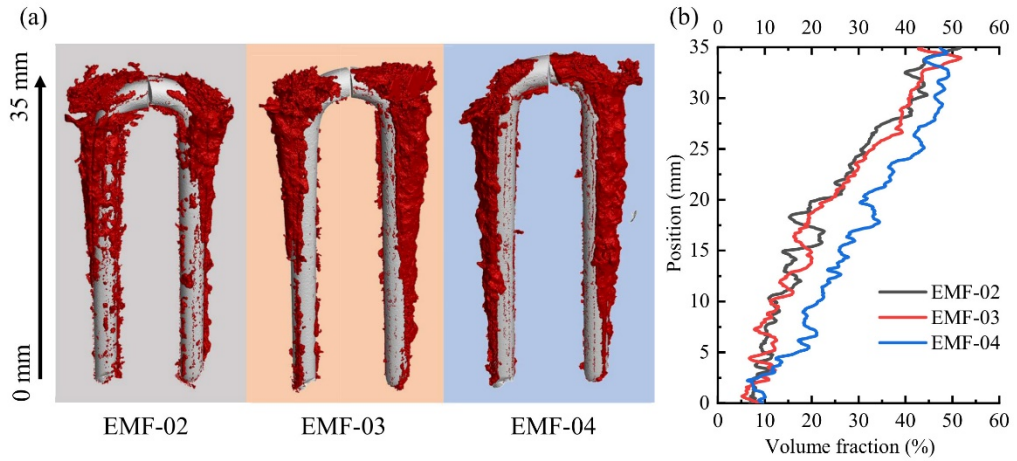

Figure 3 (a) 3D structure of a ROI containing rebar (gray), cement matrix (transparent), and pores (red); (b) changes of volume fraction of the defects in EMF-02, EMF-03 and EMF-04.

The volume and fraction of the gaps (or defects) around the saddle stitches in EMFs are shown in **Figure 4**. The volumes in each sample were above 100 mm^3. As the viscosity of the EMF slurries increased from 14 Pa·s to 20 Pa·s, the defects' volume increased from 120.60 mm^3 to 139.51 mm^3 (Figure 4a). The fraction of the defects to rebars in the same ROIs was calculated (**Figure 4b)**. The volume fractions of the defects were 23.20%, 23.81% and 30.57%, for EMF-02, EMF-03 and EMF-04, respectively.

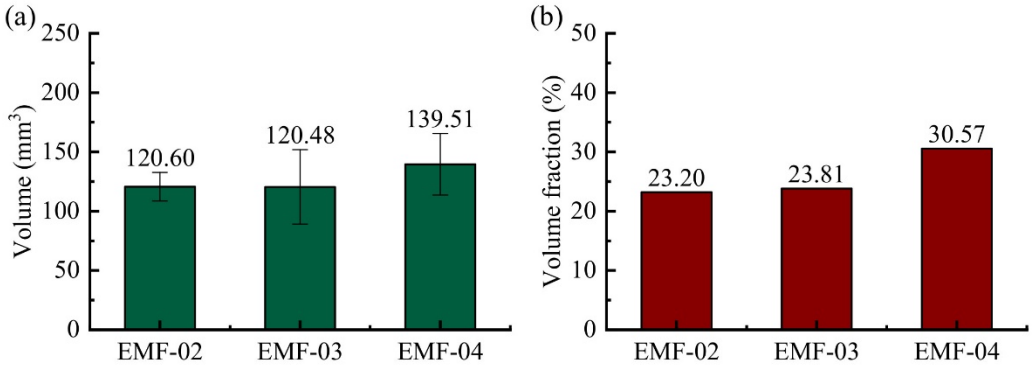

Figure 4 The result of (a) volume and (b) volume fraction of defects.

In a word, in EMFs with implanted rebars, defects were easier to form around the post-implanted saddle stitches. More defects were observed at the top of the EMFs and for the slurries with higher viscosity. The shearing action during implantation and high cohesive force of cement slurries may account for the special distribution of defects. During implantation, the surrounding cement slurries was subjected to the shearing action by the rebars and the cement slurries around the implantation path would be peeled off. Different from ordinary cement slurries, the high cohesive force of the 3D-printed slurry prevents the adjacent cement slurries from flowing and filling the gaps around the rebars. Moreover, the distance between two

branches of the saddle stitches decreases, so pressing occurred to the materials at the inboard of the U-shape rebars, and larger gaps formed at the outboard as the rebars progressively penetrated into the EMFs (Figure 3a).

4 Conclusion

In EMFs, defects were probed between post-implanted saddle stitches and cement matrix by XCT. More defects appeared at the top of the EMFs, at the outboard of the rebars, and for the cement slurries with higher viscosity.

Acknowledgements

This work was supported by the Program Fund of Non-Metallic Excellence and Innovation Center for Building Materials (2022SFP1-1).

References

Aleksejev J., Williamson M., Huber J.E., Magdysyuk O.V., Michalik S., Marrow T.J. (2022). *Use of synchrotron X-rays for direct observation of wear damage in optically-opaque contacts by means of CT imaging and X-ray diffraction*, Tribology International, 175, 107809.

Arunothayan A.R., Nematollahi B., Ranade R., Bong S.H., Sanjayan J.G., Khayat K. H. (2021) *Fiber orientation effects on ultra-high performance concrete formed by 3D printing*, Cement and Concrete Research, 143, 106384.

Cao X., Yu S., Zheng D., Cui H. (2022). *Nail planting to enhance the interface bonding strength in 3D printed concrete*, Automation in Construction, 141, 104392.

Ding T., Xiao J., Zou S., Wang Y. (2020). *Hardened properties of layered 3D printed concrete with recycled sand*, Cement and Concrete Composites, 113, 103724.

Li Z., Ma G., Wang F., Wang L., Sanjayan J. (2022). *Expansive cementitious materials to improve micro-cable reinforcement bond in 3D concrete printing*, Cement and Concrete Composites, 125, 104304.

Lu B., Weng Y., Li M., Qian Y., Leong K. F., Tan M. J., Qian S. (2019). *A systematical review of 3D printable cementitious materials*, Construction and Building Materials, 207, 477-490.

Nerella V.N., Hempel S., Mechtcherine V. (2019) *Effects of layer-interface properties on mechanical performance of concrete elements produced by extrusion-based 3D printing*, Construction and Building Materials, 205, 586–601.

Sun X., Zhou J., Wang Q., Shi J., Wang H. (2022). *PVA fibre reinforced high-strength cementitious composite for 3D printing: Mechanical properties and durability,* Additive. Manufacturing, 49, 102500.

Wang L., Tian Z., Ma G., Zhang M. (2020). *Interlayer bonding improvement of 3D printed concrete with polymer modified mortar: experiments and molecular dynamics studies*, Cement and Concrete Composites, 110, 103571.

Wang L., Ma G., Liu T., Buswell R., Li Z. (2021). *Interlayer reinforcement of 3D printed concrete by the in-process deposition of U-nails*, Cement and Concrete Research, 148, 106535.

Yang R., Zeng Q., Peng Y., Wang H., Wang Z. (2022). *Anomalous matrix and interlayer pore structure of 3D-printed fiber-reinforced cementitious composites*, Cement and Concrete Research, 157, 106829.

Yang R., Zhu Y., Lan Y., Zeng Q., Peng Y., Wang Z. (2022). *Differences in micro grain/fiber distributions between matrix and interlayer of cementitious filaments affected by extrusion molding*, Additive Manufacturing, 60, 103236.